

Production of Silicon on Mass Increasing White Dwarfs – Possible Origin of High-Velocity-Features in Type Ia Supernovae

MARIKO KATO,¹ HIDEYUKI SAIO,² AND IZUMI HACHISU³

¹*Department of Astronomy, Keio University, Hiyoshi, Yokohama 223-8521, Japan;*

²*Astronomical Institute, Graduate School of Science, Tohoku University, Sendai, 980-8578, Japan*

³*Department of Earth Science and Astronomy, College of Arts and Sciences, The University of Tokyo, 3-8-1 Komaba, Meguro-ku, Tokyo 153-8902, Japan*

ABSTRACT

Type Ia supernovae (SNe Ia) often show high-velocity absorption features (HVF) in their early phase spectra; however the origin of the HVF is unknown. We show that a near-Chandrasekhar-mass white dwarf (WD) develops a silicon-rich layer on top of a carbon-oxygen (CO) core before it explodes as an SN Ia. We calculated the nuclear yields in successive helium shell flashes for 1.0 M_{\odot} , 1.2 M_{\odot} , and 1.35 M_{\odot} CO WDs accreting helium-rich matter with several mass-accretion rates ranging from $1 \times 10^{-7} M_{\odot} \text{ yr}^{-1}$ to $7.5 \times 10^{-7} M_{\odot} \text{ yr}^{-1}$. For the 1.35 M_{\odot} WD with the accretion rate of $1.6 \times 10^{-7} M_{\odot} \text{ yr}^{-1}$, the surface layer developed as helium burning ash and consisted of 40% ^{24}Mg , 33% ^{12}C , 23% ^{28}Si , and a few percent of ^{20}Ne by weight. For a higher mass accretion rate of $7.5 \times 10^{-7} M_{\odot} \text{ yr}^{-1}$, the surface layer consisted of 58% ^{12}C , 31% ^{24}Mg , and 0.43% ^{28}Si . For the 1.2 M_{\odot} WDs, silicon is produced only for lower mass accretion rates (2% for $1.6 \times 10^{-7} M_{\odot} \text{ yr}^{-1}$). No substantial silicon ($< 0.07\%$) is produced on the 1.0 M_{\odot} WD independently of the mass-accretion rate. If the silicon-rich surface layer is the origin of Si II HVFs, its characteristics are consistent with that of mass increasing WDs. We also discuss possible Ca production on very massive WDs ($\gtrsim 1.38 M_{\odot}$).

Keywords: nova, cataclysmic variables – stars: individual (V445 Pup) – supernova – white dwarfs

1. INTRODUCTION

Type Ia supernovae (SNe Ia) are thought to be thermonuclear explosions of a carbon-oxygen (CO) white dwarf (WD) in a close binary system. However, the exact nature of the progenitor binary system and the details of the explosion mechanism are still being debated.

Many SNe Ia show high velocity absorption lines of Ca II near-infrared (NIR) triplet and Si II $\lambda 6355$ (Mazzali et al. 2005; Childress et al. 2014; Zhao et al. 2015, 2016) before or near B maximum. Their line velocities are faster by $\sim 6000 \text{ km s}^{-1}$ or more than the photospheric velocity; hence, these high-velocity lines are referred to as high-velocity features (HVF). Several ideas on the origin of HVF have been proposed. These ideas are associated with one of (1) Ca and Si abundance enhancements in the outermost layer of the ejecta, (2) density enhancement caused by swept-up material, and (3) ionization enhancement in the outermost layer of the

ejecta (see, e.g., Gerardy et al. 2004; Mazzali et al. 2005; Tanaka et al. 2006). This is because the outermost layers of SNe Ia ejecta have the fastest expansion velocities (e.g., Figure 4 of Gerardy et al. 2004), the velocities of which are much faster than the bulk of intermediate elements near the photosphere.

The origin of HVF provides the nuclear burning process of SNe Ia, especially in the outermost layers of the ejecta, and elucidates the exact nature of their immediate progenitors. In the present paper, we examine a possible origin of the aforementioned abundance enhancement (1), that is, the nuclear burning yields in helium shell flashes on massive CO WDs as proposed by Kamiya (2012) and present the chemical composition of the outermost layer of progenitor WDs. If all the mass-increasing WDs that will explode as an SN Ia have developed silicon-rich layer on top of the CO core, it may explain the nature of Si II $\lambda 6355$ HVFs.

Two major progenitor scenarios of SNe Ia have been proposed so far (e.g., Maoz et al. 2014). One is the single-degenerate (SD) model, for which the binary system consists of a WD and a non-degenerate star like

the main-sequence star, and the other is the double-degenerate (DD) model, which consists of two WDs. There are many immediate progenitor models of the SD scenario presented so far, including a WD with steady hydrogen burning, a recurrent nova (unstable hydrogen burning), and helium nova that accretes helium-rich material from a hydrogen-deficient companion. In the former two cases, hydrogen burning produces helium ash underneath the hydrogen burning zone, and a helium flash occurs when the helium layer satisfies the ignition condition. Thus, many accreting WDs experience helium shell flashes and nuclei heavier than carbon are inevitably yielded and accumulate on the CO core. The aim of this paper is to study helium nuclear burning products for various WD masses and mass accretion rates, and to show that mass-accreting WDs are a possible production site of Si, which could be the origin of Si II $\lambda 6355$ HVFs.

Herein, we concentrate on helium-rich matter accretion, because in the presence of hydrogen, a few hundred H-flashes should occur between two consecutive He-flashes, which causes our calculations to be extremely time-consuming. Instead, we assume that the WD accretes hydrogen-deficient matter. This paper is organized as follows; we first briefly describe our numerical method in Section 2. Our numerical results are presented in Section 3. In Section 4, we propose a production site for Si II $\lambda 6355$ HVFs. In Section 5, we present nuclear yield results of helium novae and chemical composition of the ejecta. The discussion and conclusions follow in Sections 6 and 7, respectively.

2. NUMERICAL METHOD

We have calculated successive He shell flashes. The details of our numerical code and calculation method are published in Kato et al. (2017a,b). Nucleosynthesis in the helium burning is calculated up to ^{28}Si , in which nuclear reaction rates and Q-values are obtained from Caughlan & Fowler (1988), screening factors are obtained from Graboske et al. (1973). Neutrino emissions not related to the nuclear reactions are obtained from the formulae of Itho et al. (1989). Coulomb effects in the equation of state in the dense core are included using the empirical equations obtained by van Horn (1971).

The WD masses and mass accretion rates are summarized in Table 1 and also indicated by the filled red stars in Figure 1. Multicycle nova outbursts were calculated using a Henyey-type evolution code. The code encounters numerical difficulties when the nova envelope expands to a giant size. To continue numerical calculations beyond the extended stage, we adopted numerical mass loss schemes because during the extended stages

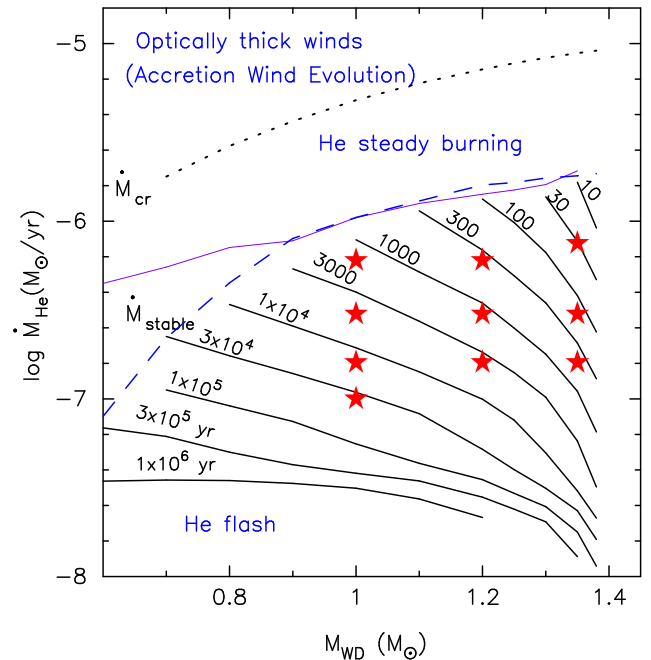


Figure 1. The response of WDs on the mass accretion rate. The chemical composition of the accreted matter is $Y = 0.98$ and $Z = 0.02$. Helium flashes occur below the stability line of He-burning (\dot{M}_{stable} : dashed line). The loci of equi-recurrence period are plotted together with its recurrence period. Between the two lines of \dot{M}_{cr} and \dot{M}_{stable} , the He nuclear burning rate is the same as the mass-accretion rate. In the region above the dotted line (\dot{M}_{cr}), the optically thick winds are accelerated and the binary undergoes accretion wind evolution (Hachisu et al. 1996, 1999a,b). The red stars indicate the models in Table 1. We added the stability line obtained by Wang et al. (2017) (thin solid line). See Section 6.4 for more details.

of nova outbursts, optically-thick wind mass-loss occurs (e.g., Kato & Hachisu 1994). To avoid the complicated iteration process of wind fitting (that gives the proper wind mass-loss rate), we simply assume a mass-loss formula during the extended stage (Kato et al. 2017a).

We obtained mass loss rates as

$$\dot{M}^{n+1} = \dot{M}^n (R_{\text{ph}}^n / R_{\text{ph}}^{n-1})^a, \quad (1)$$

where \dot{M}^{n+1} is the numerical mass-loss rate and R_{ph}^{n+1} the photospheric radius for $(n+1)$ time-step. To calculate mass-loss stages successfully we chose a parameter a as 4, 3, and 2 for $M_{\text{WD}} = 1.0, 1.2,$ and $1.35 M_{\odot}$, respectively. The initial mass loss rates were chosen as -10^{-7} and $-10^{-6} M_{\odot} \text{ yr}^{-1}$. We started the mass loss when the photospheric radius expanded to the given value, $\log(R_0/R_{\odot}) = -1.1$ to -1.3 , and its rate increases with time. The mass loss rate decreases as the radius becomes smaller. We stop the mass loss when the radius becomes smaller than the given value, $\log(R_1/R_{\odot}) = -1.5$ to

–1.4. The maximum mass-loss rate for each model is given in Table 1.

Table 1 summarizes our model parameters. The first column shows the model name, i.e., M10.6 means that the WD mass is $1.0 M_{\odot}$ with the mass accretion rate of $6 \times 10^{-7} M_{\odot} \text{ yr}^{-1}$. Then, the table lists the WD mass, mass accretion rate, maximum mass-loss rate, number of the flash cycles we calculated, the recurrence period which is defined as the time between the epochs of maximum nuclear luminosity, accreted mass, flash duration, maximum nuclear luminosity $L_{\text{nuc}}^{\text{max}}$, the maximum temperature $T_{\text{max}}^{\text{max}}$ at one cycle of shell flash (i.e., the maximum of T_{max}), and the maximum temperature T_{max}^* of the plane-parallel atmosphere, which is explained later in Equation (3).

We assume that the CO core is composed of 48% of ^{12}C , 50% of ^{16}O , and 2% of ^{24}Mg by weight. This assumption does not affect our results, because the CO core material hardly mixes with the upper part and the newly accreted matter is burned into heavy elements and accumulates on the surface of CO core. Our nuclear network includes 14 isotopes, i.e., ^1H , ^3He , ^4He , ^{12}C , ^{13}C , ^{14}N , ^{15}N , ^{16}O , ^{17}O , ^{18}O , ^{20}Ne , ^{22}Ne , ^{24}Mg , and ^{28}Si coupled by 21 reactions. This nuclear network is small enough to efficiently speed up the time-consuming calculation of a number of shell flashes, but covers all the main paths of nuclear reactions for both energy and nuclide productions. The resultant nuclei distribution is in good agreement with other calculations which include much larger networks as will be discussed in Section 6.2.

Figure 1 shows the response of WDs for the He mass-accretion rate vs. WD mass, which is the so-called Nomoto diagram (Nomoto 1982). Here, we assume that the accreting matter is helium-rich and has the composition of helium $Y = 0.98$ and heavy elements $Z = 0.02$ by weight, where Z includes the solar composition of elements heavier than helium. Under the stability line, helium shell-burning is unstable and periodic helium nova outbursts occur. Between the stability line (\dot{M}_{stable}) and the line denoted by \dot{M}_{cr} , helium shell-burning is stable with the consumption rate being the same as the mass-accretion rate. Above the line of \dot{M}_{cr} , optically thick winds are accelerated and the WD undergoes accretion wind evolution, in which the WD accretes matter from the accretion disk and, at the same time, the WD loses mass from the other direction in the wind (see, e.g., Figure 1 of Hachisu & Kato 2001). Our calculated models correspond to the WD masses and mass-accretion rates indicated with the filled red stars. We discuss the stability line in Section 6.4.

Although we started our calculation close to the thermal equilibrium model (Nomoto et al. 2007; Kato et al.

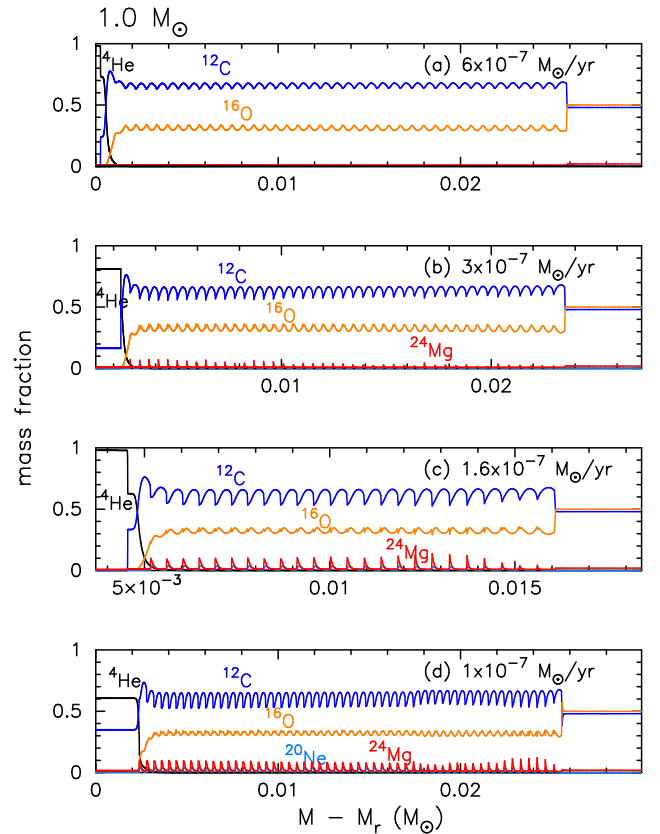


Figure 2. Mass fraction of ^{12}C (blue), ^{16}O (orange), ^{20}Ne (cyan-blue), and ^{24}Mg (red) in the surface region around the $1.0 M_{\odot}$ CO WD in very late stages of He flashes when the accretion has restarted. The surface is toward the left while the WD center is toward the right. (a) M10.6. (b) M10.3. (c) M10.16. (d) M10.1. The mass-accretion rates are depicted in each panel.

2014), the recurrence periods (red stars) in Table 1 are slightly longer than those (black lines) in Figure 1, because our time-dependent shell flash models have not yet reached a limit cycle. For example, model M10.1 has $P_{\text{rec}} = 79500$ yr in the 23th cycle but $P_{\text{rec}} = 74200$ yr in the 55th cycle. We stopped our calculation before P_{rec} reach the limit cycle because it converges very slowly (Kato et al. 2017b).

3. RESULTS

3.1. $1.0 M_{\odot}$ WD

Figure 2 shows the abundance of various nuclear yields in the surface region of the $1.0 M_{\odot}$ WD with the four different mass accretion rates. The photosphere is toward the left while the WD center is toward the right. There are 41, 43, 25, and 55 small wavy variations in the carbon and oxygen profiles, corresponding to the temperature variation during the previous successive helium shell flashes in each model. Carbon ($X(^{12}\text{C}) \sim 0.6$) and

Table 1. Model parameters of He shell flashes

Model	M_{WD}	\dot{M}_{acc}	$\dot{M}_{\text{ML}}^{\text{max}}$	Cycle	P_{rec}	M_{acc}	Flash ^a	$L_{\text{nuc}}^{\text{max}}$	$\log T_{\text{max}}^{\text{max}}$	$\log T_{\text{max}}^*$
	(M_{\odot})	($M_{\odot}\text{yr}^{-1}$)	($M_{\odot}\text{yr}^{-1}$)		(yr)	(M_{\odot})	(yr)	(L_{\odot})	(K)	(K)
M10.6	1.0	6.0×10^{-7}	1.2×10^{-5}	41	1270	7.4×10^{-4}	165	2.5×10^7	8.54	8.56
M10.3	1.0	3.0×10^{-7}	8.8×10^{-5}	44	7330	2.2×10^{-3}	111	6.2×10^9	8.66	8.72
M10.16	1.0	1.6×10^{-7}	4.4×10^{-4}	25	31800	5.1×10^{-3}	101	2.6×10^{11}	8.74	8.83
M10.16.T ^b	1.0	1.6×10^{-7}	1.6×10^{-2}	13	35300	5.6×10^{-3}	56.0	3.5×10^{11}	8.74	8.84
M10.1	1.0	1.0×10^{-7}	1.3×10^{-3}	55	74200	7.4×10^{-3}	89.0	1.5×10^{12}	8.78	8.89
M12.6	1.2	6.0×10^{-7}	1.8×10^{-5}	20	444	2.6×10^{-4}	27.3	7.1×10^7	8.62	8.63
M12.3	1.2	3.0×10^{-7}	5.1×10^{-5}	21	1990	5.9×10^{-4}	25.0	3.3×10^9	8.71	8.74
M12.16	1.2	1.6×10^{-7}	2.8×10^{-4}	27	9340	1.5×10^{-3}	21.4	2.5×10^{11}	8.81	8.85
M135.75	1.35	7.5×10^{-7}	5.3×10^{-6}	14	34.1	2.5×10^{-5}	3.42	5.0×10^6	8.66	8.64
M135.3	1.35	3.0×10^{-7}	1.7×10^{-5}	29	203	6.0×10^{-5}	4.29	5.0×10^8	8.74	8.73
M135.16	1.35	1.6×10^{-7}	3.5×10^{-5}	15	743	1.2×10^{-4}	4.90	8.5×10^9	8.82	8.81

^a The flash duration is defined by the period during which $L_{\text{ph}} > 10^4 L_{\odot}$.

^b A test model with extremely large mass-loss rate.

Table 2. Mass Fractions of Nuclear Products

Model	^{12}C	^{16}O	^{20}Ne	^{24}Mg	$^{28}\text{Si}^a$
M10.6	0.66	0.31	0.0029	0.0088	8.1×10^{-4}
M10.3	0.64	0.33	0.0082	0.012	8.3×10^{-4}
M10.16	0.62	0.33	0.016	0.026	9.9×10^{-4}
M10.1	0.60	0.32	0.019	0.035	1.5×10^{-3}
M12.6	0.59	0.24	0.064	0.087	9.5×10^{-4}
M12.3	0.56	0.12	0.064	0.24	3.6×10^{-3}
M12.16	0.53	0.087	0.054	0.30	0.020
M135.75	0.58	0.045	0.045	0.31	0.0043
M135.3	0.42	0.014	0.021	0.46	0.069
M135.16	0.33	0.0087	0.014	0.40	0.23

^a Including pre-existing Si in the accreted matter $X(\text{Si})=8.1 \times 10^{-4}$.

oxygen ($X(^{16}\text{O}) \sim 0.3$) are the most abundant elements, which are almost independent of the mass accretion rate. Helium shell flashes produce small amounts of ^{24}Mg and ^{28}Si at lower mass-accretion rates. The average mass fractions of each element in the wavy profile region are summarized in Table 2.

Figure 3 shows the temporal changes of the temperature and density at the point of maximum temperature in the helium-rich ($Y > 0$) region during the last cycle of helium shell flashes (the 23th cycle for the $1.0 \times 10^{-7} M_{\odot} \text{yr}^{-1}$ case). The time from the onset of the flash ($t = 0$ defined at $L_{\text{nuc}} = L_{\text{nuc}}^{\text{max}}$) is indicated on the curves in units of year unless otherwise specified. The maximum temperature quickly rises in a timescale of 0.1 yr until $t = 0$. Then, it moves leftward as the envelope begins to expand. Mass-loss occurs in the dotted part. After the maximum expansion, the inner part of the envelope turns to shrink. When the photospheric radius

shrinks to $\log R_{\text{ph}}/R_{\odot} = -1.25$, the mass loss stops. Shortly afterward, the WD envelope reaches a plane-parallel hydrostatic structure and the maximum temperature is almost constant ($\log T$ (K) ~ 8.47 - 8.5) for several tens of years ($t > 60$ yr). This phase corresponds to the supersoft X-ray source (SSS) phase ($\log T_{\text{ph}} \sim 5.5$). When the helium-rich envelope mass ($M_{\text{He}} = \int dM_r$ for $Y > 0$) decreases and cannot maintain the temperature sufficiently high for He-burning, the flash ends. In the post-flash phase, the temperature of envelope ($Y > 0$) decreases and the maximum temperature shifts to the inner part of the shell ($Y = 0$ region). Therefore, in this figure, we plot both the temperature, i.e., the maximum temperature (thick solid lines) of the whole WD and the temperature (thin solid lines) at the bottom of helium shell. The next outburst ignites in the mid of the helium-rich region ($Y > 0$); hence, the locus of cycles does not close after one cycle of flashes.

In Figure 3, a smaller mass-accretion rate model makes a larger cycle (locus), because the ignition mass is larger for a low mass-accretion rate, and thus, the temperature at the nuclear burning region reaches a higher value. The accreted mass M_{acc} before ignition, and the maximum temperature $T_{\text{max}}^{\text{max}}$ for each cycle are summarized in Table 1.

Figures 4 and 5 show the temporal change of the nuclear products in the very surface region. Before the He flash sets in, freshly accreted matter of $Y = 0.98$ is on top of the leftover of previous outburst where the helium mass fraction gradually decreases from $Y = 0.62$ to zero. Unstable He-burning sets in at the boundary of these two regions and the burning region quickly extends upward by convection. Figure 4(a) shows a stage shortly after the onset of He flash ($t = 5.8$ min). The

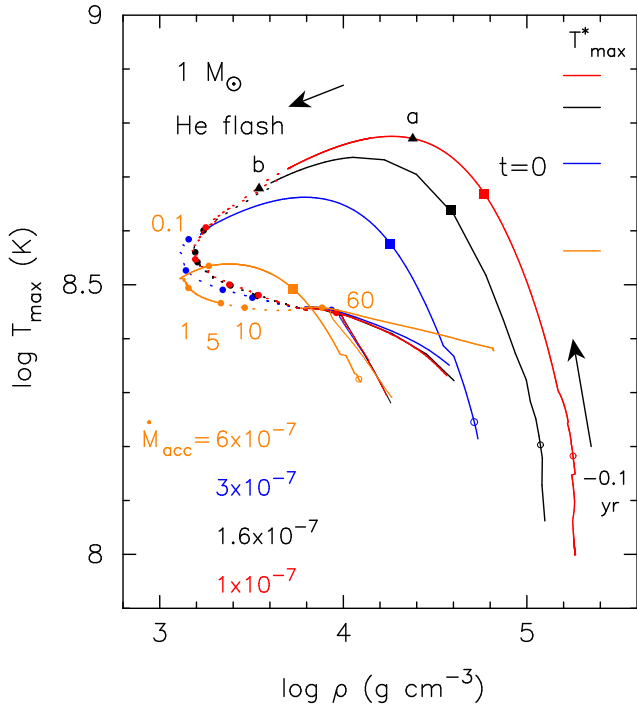


Figure 3. Locus of the maximum temperature (T_{\max}) and its density for one cycle of our helium flash calculation on the $1.0 M_{\odot}$ WD for various mass-accretion rates. The origin (zero) of time is set at the onset of shell flashes ($L_{\text{nuc}} = L_{\text{nuc}}^{\max}$ at $t = 0$). The indicated time is $t = -0.1$ yr (open circles), 0.0 (filled squares), 0.1, 1, 5, 10, and 60 yr (five dots, respectively). Stages labeled a and b (filled black triangles) correspond to those in Figure 4. The mass loss phase is denoted by the dotted line. After the mass loss phase, the nova enters the supersoft X-ray source (SSS) phase in which the different models undergo a similar path until $t \sim 60$ yr. Shortly after, the place of maximum temperature shifts inward ($Y = 0$ region). Thus, we indicate the maximum temperature for the whole WD (thick solid line) as well as the temperature at the bottom of the He layer ($Y > 0$ region, thin solid line). The end point of the line is the epoch when the nuclear luminosity drops to $L_{\text{nuc}} = 100 L_{\odot}$. The next outburst occurs in the middle of the helium layer ($Y > 0$), thus, these cycles do not close in this plot.

high-temperature region (nuclear burning region) extends upward (toward the left in Figure 4) from the boundary. As triple- α reaction converts ${}^4\text{He}$ into ${}^{12}\text{C}$, the helium mass fraction decreases with time, keeping a constant value with convective mixing in Figure 4(a)–(c) and Figure 5(d). With the progression of time, the high-temperature region gradually extends inward and reaches zone 2 within 1 yr and zone 3 within 5 yr. The leftover helium in zone 2 is consumed by nuclear reactions and is exhausted until the end of the shell flash. Here, the zone number corresponds to the cycle number of helium shell flashes from the recent one.

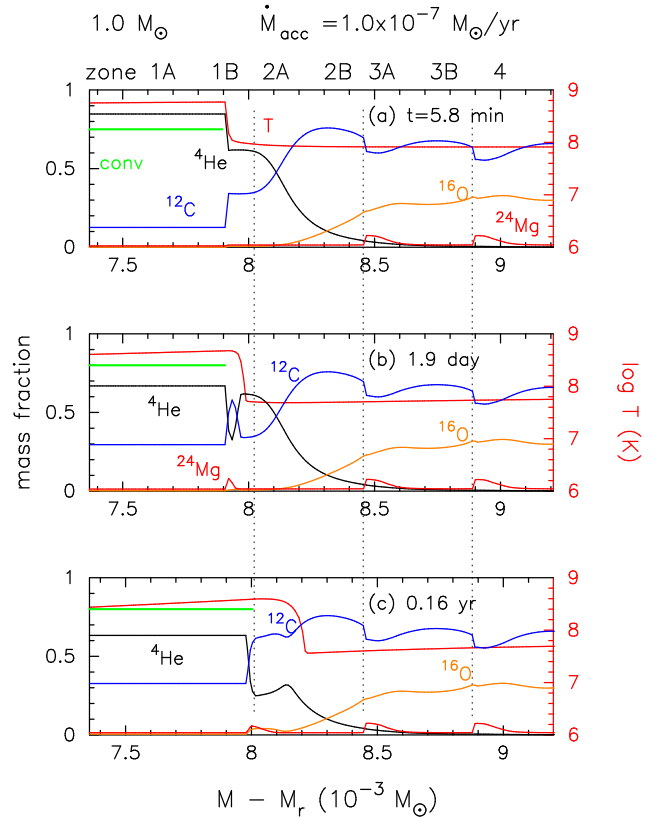


Figure 4. Distributions of the temperature (upper red solid line), ${}^4\text{He}$ (black solid), ${}^{12}\text{C}$ (blue solid), ${}^{16}\text{O}$ (orange solid), and ${}^{24}\text{Mg}$ (lower red solid line) of the surface region for several selected early phases of a He flash on the $1.0 M_{\odot}$ WD. The convective region is indicated by the horizontal thick green line.

Figure 4 shows that carbon is synthesized by the triple- α reaction in zones 1B and 2A in an early phase of $t < 1$ yr. A large part of the carbon produced in zone 1B is carried outward by convection to increase the carbon mass fraction to $X({}^{12}\text{C}) \gtrsim 0.3$. Correspondingly, the helium fraction decreases to $Y \sim 0.6$. The carbon mass fraction in zone 1B increases after the convection disappears, i.e., the envelope becomes radiative, because the temperature is still as high as $\log T$ (K) > 8.4 . This carbon remains until the next outburst.

The oxygen mass fraction in zones 1 and 2 increases in the later phase (see Figure 5) through an α -capture reaction, ${}^{12}\text{C}(\alpha, \gamma){}^{16}\text{O}$, that continues until the end of the flash. Thus, ${}^{16}\text{O}$ mass fraction shows wavy variation almost in anti-phase to that of ${}^{12}\text{C}$ (see also Figure 18 for a wider mass range of the envelope).

Magnesium is produced only at the higher temperature of $\log T_{\max}$ (K) > 8.55 , thus, it occurred only in an early phase. Figure 4(b) and (c) show that ${}^{24}\text{Mg}$ produced in zone 1B is carried outward by convection.

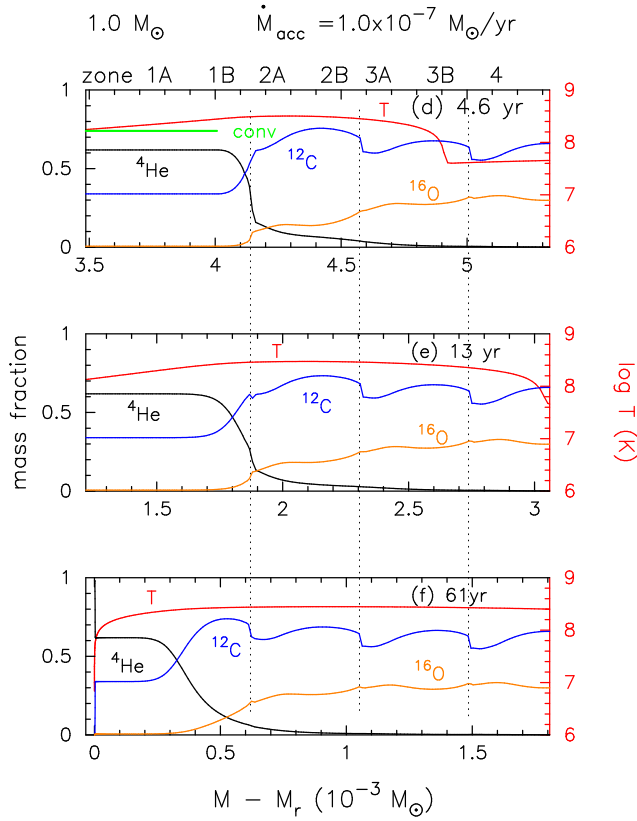


Figure 5. Same as Figure 4, but for later phases, and ^{24}Mg is omitted for simplification. The mass coordinate is shifted leftward in these stages because the envelope mass decreased due to mass loss. Mass-accretion restarts in stage (f).

Only magnesium formed in zone 2A (the radiative region) remains after the end of the outburst.

3.2. $1.2 M_{\odot}$ WD

Figure 6 shows the temporal change of the maximum temperature and its density in the He-rich envelope during the last cycle of our $1.2 M_{\odot}$ WD with three different mass-accretion rates. The characteristic properties are the same as those of the $1.0 M_{\odot}$ WD in Figure 3. The maximum temperature is higher than that of the $1.0 M_{\odot}$ WD with the same accretion rate, due to a larger gravity, despite the smaller ignition mass. The flash durations are much shorter than those in the $1.0 M_{\odot}$ WD, but the higher temperature ($\log T_{\max} (\text{K}) > 8.6$) continues for a much longer time (1 yr). Therefore, the α -process produces more massive nuclei. Figure 7 and Table 2 show $X(^{12}\text{C}) \sim 0.55$ and $X(^{16}\text{O}) \sim 0.1 - 0.25$, both of which are smaller than those in the $1.0 M_{\odot}$ WD, but more ^{24}Mg is produced.

Figure 8(b) and (c) show that the ^{24}Mg and ^{28}Si produced in zone 1B are carried out by convection and mixed into the He-rich envelope. In zone 2A, the radiative zone, the ^{24}Mg fraction increases until $t = 1$ yr.

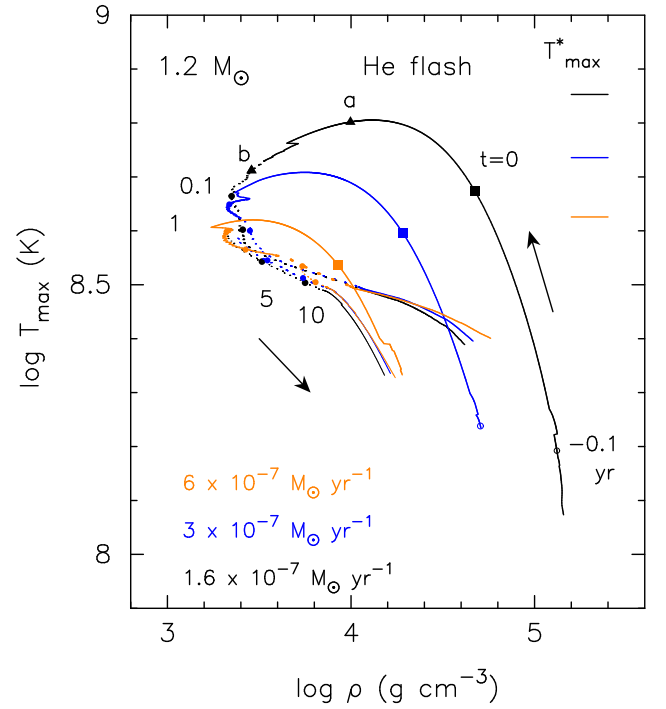


Figure 6. Same as Figure 3, but for the $1.2 M_{\odot}$ WDs with the three mass-accretion rates. In model M12.16 (black line), the filled black triangles labeled a and b correspond to the stages (a) and (b), respectively, in Figure 8.

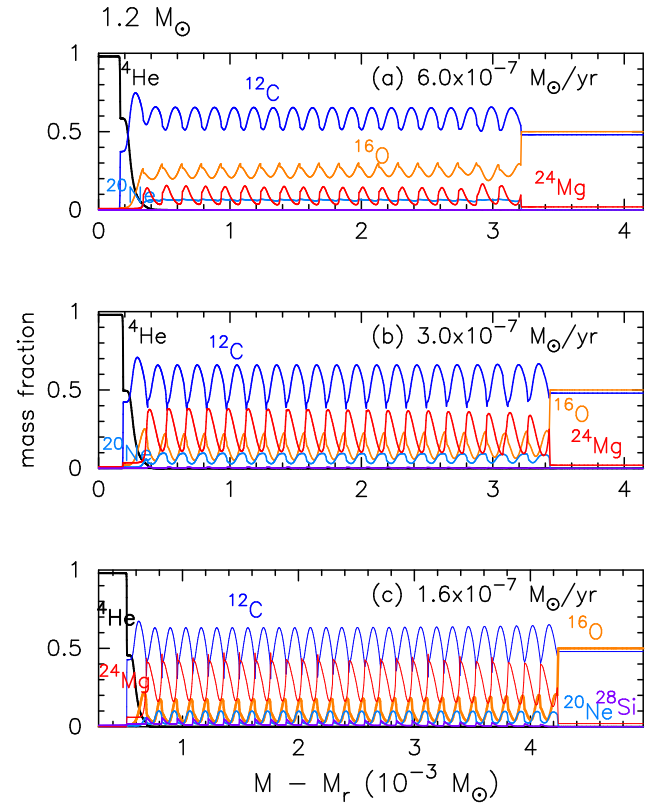


Figure 7. Same as Figure 2, but for the $1.2 M_{\odot}$ WD.

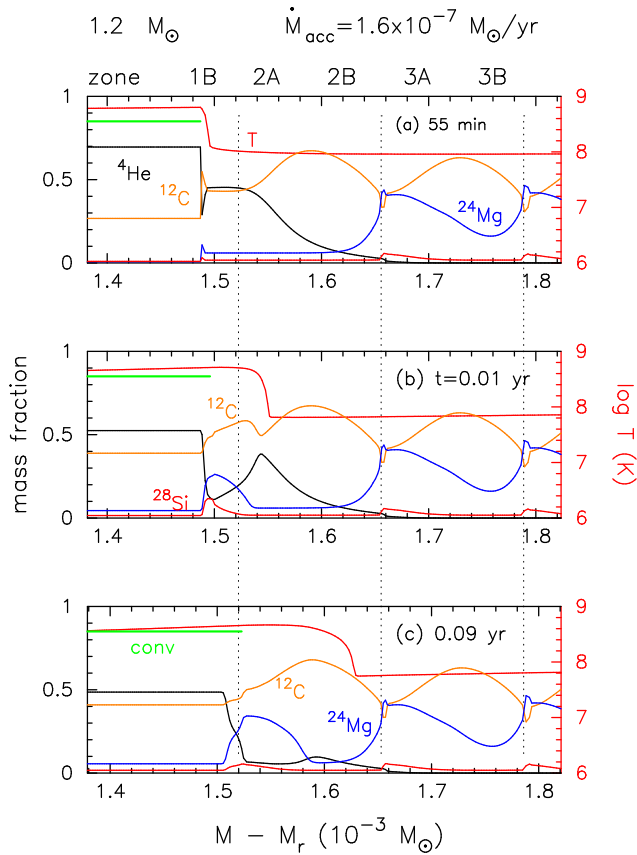


Figure 8. Same as Figure 4, but for the model of M12.16. Note that we used different color to Figure 7 to distinguish carbon and He lines: ^4He (black), ^{12}C (orange), ^{24}Mg (blue), and ^{28}Si (lower red).

Only a small amount of ^{28}Si is produced (see Table 2), because it is produced by the reaction $^{24}\text{Mg} + \alpha \rightarrow ^{28}\text{Si}$ for the high temperatures of $\log T_{\text{max}} (\text{K}) > 8.7$ which does not last long in the $1.2 M_{\odot}$ models.

In stages (e), (f), and after, the envelope (zone 1B) becomes radiative. The temperature decreases but is still high, $\log T (\text{K}) \sim 8.5$, so triple- α and α -chain reactions, $^{12}\text{C}(\alpha, \gamma)^{16}\text{O}$, $(\alpha, \gamma)^{20}\text{Ne}$ produces ^{12}C , ^{16}O , and ^{20}Ne (not plotted) in zone 1B. The temperature is not high enough to produce ^{24}Mg . Thus, the carbon and magnesium mass fractions show anti-correlation as shown in Figure 7. After stage (f), the temperature decreases and the shell flash ends. The composition profile in zones 3 and 4 does not change even though the heat flux passed through inward, because there is no He nuclei and α -chain reaction does not occur.

3.3. $1.35 M_{\odot}$ WD

Figure 10 shows the temporal change of T_{max} for the three models of $1.35 M_{\odot}$ WD. The three models, M135.16, M135.3, and M135.75, follow different paths in the ρ - T plane until $t \sim 1$ yr, but similar paths after

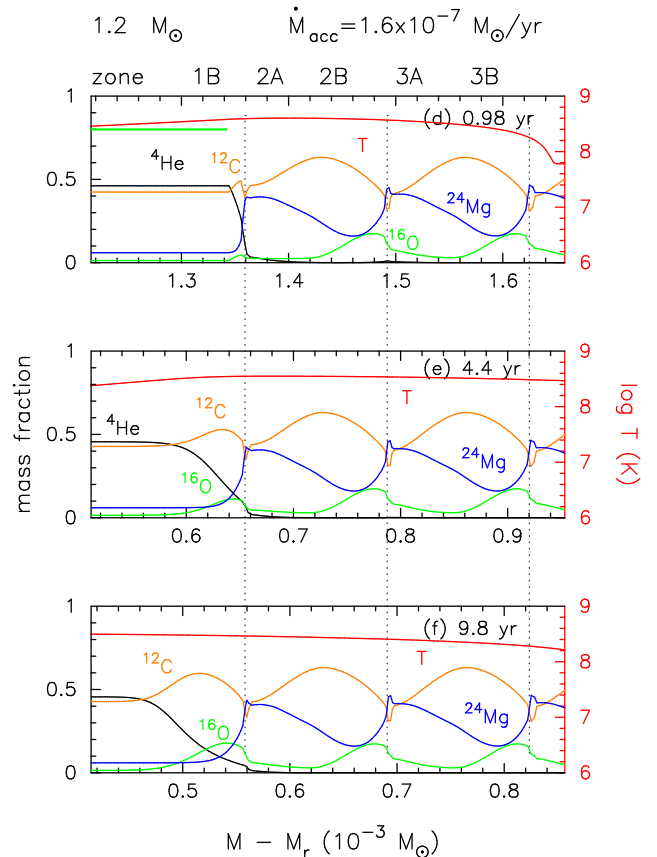


Figure 9. Same as Figure 8, but for later phases. The abundance profile of ^{16}O (lower green) is added and ^{28}Si is omitted to avoid crowdedness.

that. In model M135.16, the high temperature ($\log T_{\text{max}} (\text{K}) > 8.6$) period lasts more than two years, which is as long as half the total flash duration. This longer high-temperature period makes a substantial difference in nuclear products among the three models, as shown in Figure 11. In model M135.16, ^{24}Mg and ^{28}Si show much higher peak but less ^{12}C production.

Figures 12 and 13 present a close look at the composition profile in the surface layer for the selected stages of model M135.16. The He-shell flash started at $M - M_r = 1.18 \times 10^{-4} M_{\odot}$ and the high-temperature region widely extends upward with convection. In the hot convective region triple- α reaction converts ^4He into ^{12}C and the ^{12}C mass fraction increases. Correspondingly, ^4He decreases with time. Finally, the composition in the convective region consists of ^4He , ^{12}C , and a few percent of ^{24}Mg and ^{28}Si (see also Figure 16(b)).

The hot region extends inward much more slowly with a speed of $\lesssim 1 \times 10^{-5} M_{\odot} \text{ day}^{-1}$ as shown in Figure 12. When the temperature rises to $\log T (\text{K}) > 8.7$, the triple- α reaction and subsequent α -chain reactions up to ^{28}Si become very active in zone 2A, and as a result,

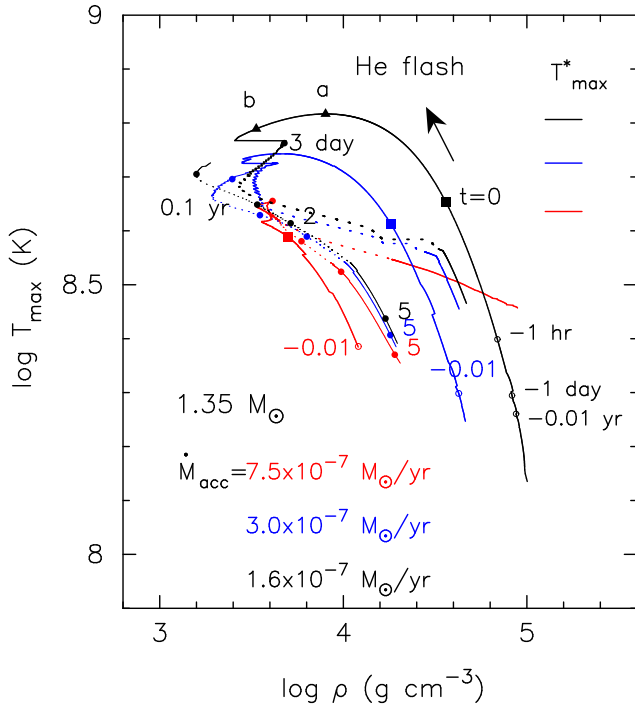


Figure 10. Same as Figure 3, but for the $1.35 M_{\odot}$ WD. The quick rightward excursion in M135.16 (black line) at $t = 3$ day is due to a jump of the place of maximum temperature when the He mass fraction at $M - M_r \sim 1.33 \times 10^{-4} M_{\odot}$ vanishes ($Y = 0$) at $t \sim 3$ day.

${}^4\text{He}$ is completely exhausted. In zone 2, ${}^{28}\text{Si}$ is mostly produced within 3 days and ${}^{24}\text{Mg}$ is produced within one month. In the inner zones, $X({}^{24}\text{Mg})$ and $X({}^{28}\text{Si})$ do not change after the temperature rises, because there is no ${}^4\text{He}$ in this region. As ${}^{28}\text{Si}$ is produced from ${}^{24}\text{Mg}$ by an α -chain reaction, ${}^{24}\text{Mg}$ decreases when ${}^{28}\text{Si}$ increases. This can be seen in the periodic anti-phase changes of ${}^{28}\text{Si}$ and ${}^{24}\text{Mg}$ in Figure 11. The mass fraction of ${}^{24}\text{Mg}$ in zone 1B increases after the region becomes radiative (see Figure 13), but ${}^{28}\text{Si}$ does not much increase. We will compare our results with other calculations including large nuclear networks in Section 6.

4. HELIUM SHELL FLASHES AS A PRODUCTION SITE OF HVFs

4.1. Production of Si

Table 2 summarizes the mean values of mass fractions of the main nuclei in the wavy composition profiles of Figures 2, 7, and 11. For the $1.0 M_{\odot}$ WD, the major products of He-burning are C and O, a few percent of Ne and Mg, and very small amount of Si ($< \text{several} \times 10^{-4}$), independent of the mass-accretion rate. For the $1.2 M_{\odot}$ WD, ${}^{24}\text{Mg}$ and ${}^{28}\text{Si}$ production rates are very sensitive to the mass-accretion rate. For the $1.35 M_{\odot}$ WD, ${}^{12}\text{C}$ and ${}^{24}\text{Mg}$ are the most abundant nuclei and the ${}^{28}\text{Si}$

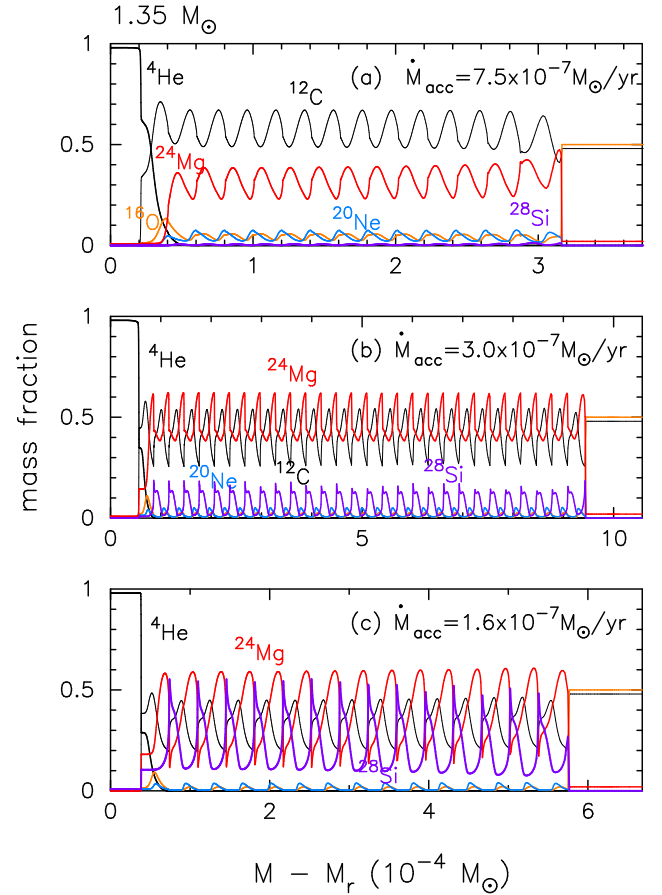


Figure 11. Same as Figure 2, but for the $1.35 M_{\odot}$ WD.

mass fraction is sensitive to the mass accretion rate. The silicon mass fraction increases with the decreasing mass-accretion rate, i.e., $X({}^{28}\text{Si}) = 3.5 \times 10^{-3}$ for $\dot{M}_{\text{acc}} = 7.5 \times 10^{-7} M_{\odot} \text{ yr}^{-1}$, 0.068 for $3 \times 10^{-7} M_{\odot} \text{ yr}^{-1}$, and 0.23 for $1.6 \times 10^{-7} M_{\odot} \text{ yr}^{-1}$. (Note that the Si mass fraction in Table 2 is the summation of the newly produced silicon and the pre-existed one in the accreted matter.) Thus, we expect more Si could be synthesized with much smaller mass-accretion rates.

Our reaction network does not include nuclei above Si. We did not find any other (multi-zone) evolution calculations involving up to Ca except for the one-zone calculations of He shell flashes. We will discuss Si and Ca production in more detail in Sections 6.6 and 6.7.

4.2. Stratified surface envelope of WDs and HVFs

In binary evolution, mass-increasing WDs experience He-shell burning either when the accreted matter is hydrogen-rich or helium-rich. In the He star channel to SNe Ia (e.g., Wang et al. 2017; Wu et al. 2017), a CO WD accretes He matter from a helium star companion and increases its mass from a lower mass of $M_{\text{WD}} \lesssim 1.06 M_{\odot}$ to a mass close to the Chandrasekhar

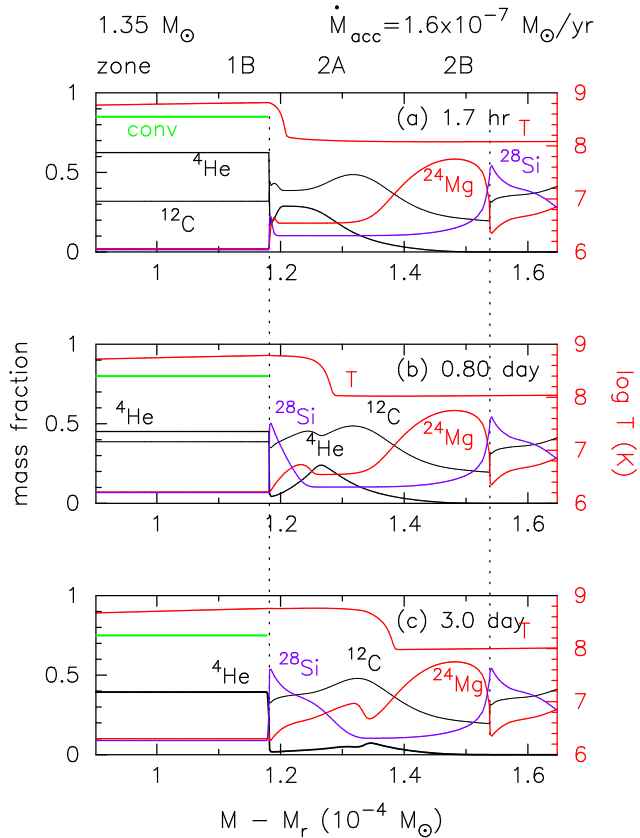


Figure 12. Same as Figure 4, but for the $1.35 M_{\odot}$ WD.

mass. During the mass increasing stage, the WD experiences steady He-burning or periodic He shell flashes, depending on the He mass-accretion rate. The He ash piles up on the CO core. The composition of the He ash depends on the WD mass and the mass accretion rate. Generally, the mass transfer rate gradually decreases as the WD mass increases with time. This is because the companion mass gradually decreases due to mass transfer. Thus, we can expect that the Si-rich layer develops when the WD is as massive as or more massive than $\sim 1.35 M_{\odot}$, and a Ca-rich layer in the envelope could develop when the WD mass approaches the Chandrasekhar mass, e.g., $\sim 1.38 M_{\odot}$. In this way, the WD develops a stratified surface layer composed of different nuclei. Typically, the most inner stratified layer, just above the CO core, is mainly composed of C and O because it was the He ash when the WD mass was $\sim 1.0 M_{\odot}$. This layer is surrounded by the Si-rich layer that is formed when the WD mass was $1.2 - 1.35 M_{\odot}$. The outermost layer could be Ca-rich when the WD grows to as massive as $\sim 1.38 M_{\odot}$ and the mass-accretion rate has decreased significantly.

When the WD finally explodes as an SN Ia, the detonation/deflagration wave goes through the WD and

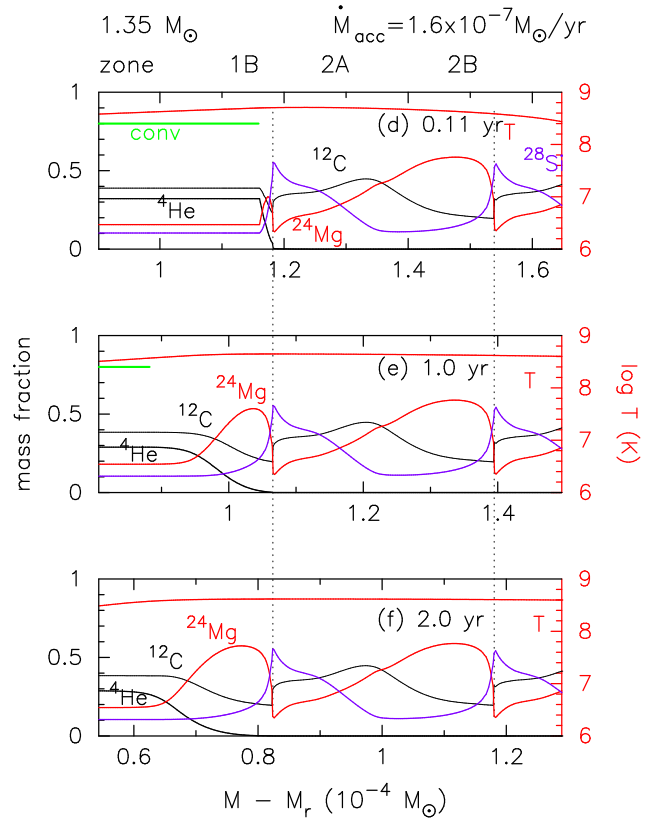


Figure 13. Same as Figure 5, but for the $1.35 M_{\odot}$ WD. Mg is produced in zone 1B.

blows up the whole WD. The blast wave activates nuclear reactions and synthesizes heavy nuclei depending on its temperature and density. When the blast wave reaches the surface, however, the temperature is reduced and is not high enough to activate nuclear reactions. Thus, the surface region remains unburnt, but is accelerated to high velocities of $\sim 23000 \text{ km s}^{-1}$ (e.g., see Gerardy et al. 2004). In this stratified envelope, the outermost Ca-rich layer receives the highest expansion velocity and the slightly inner Si-rich layer gets a smaller velocity. These surface regions could be a possible source of HVFs.

This stratification layer naturally explains the observed properties of HVFs as follows:

(1) Velocities of Ca II NIR triplet HVFs are larger by $\sim 4000 \text{ km s}^{-1}$ than that of Si II $\lambda 6355$ (Childress et al. 2014; Zhao et al. 2015, 2016). This can be explained by the stratified layer by our proposed scenario that He shell flashes produce Si-rich layer earlier than the Ca-rich layer. Thus, calcium mainly distributes in the outer layer than that of Si and, as a result, is accelerated to larger velocities.

(2) Some SNe Ia also show O I $\lambda 7773$ HVFs and its line strength is inversely correlated with that of Si II

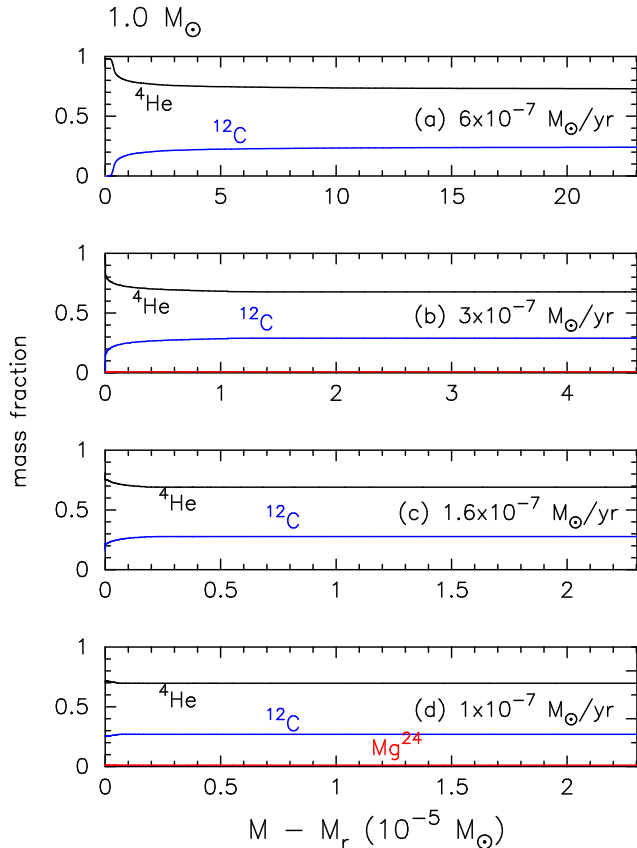


Figure 14. Mass fraction of major nuclei in the surface zone of the helium envelope just before the mass-loss sets in. The WD mass is $1.0 M_{\odot}$ with different mass-accretion rates. (a) M10.6 at $t=4.8$ yr. (b) M10.3 at $t=23$ day. (c) M10.16 at $t=1.7$ day. (d) M10.1 at $t=8.9$ hr. The surface layer of $Y = 0.98$ is very thin hence it cannot be seen in this figure except (a). In the wind phase, a part of this surface layer will be blown out.

$\lambda 6355$ (or Ca II NIR triplet) (Zhao et al. 2016). This tendency is consistent with our results as listed in Table 2.

5. EJECTA COMPOSITION IN HE NOVAE

During a He nova outburst, a part of the envelope is blown off in the wind. Figures 14, 15, and 16 show the mass fractions of major nuclei just before mass loss occurs. The surface region with $Y = 0.98$ is made of freshly accreted matter and the region underneath is the convectively mixed part during the flash. At first, the very surface layer of $Y = 0.98$ is blown off. As time goes on, the inner part will be ejected. Thus, the composition of the ejecta changes with time. From these figures, we can say that the envelope consists mainly of He and C, and slightly contaminated by Mg and Si, which depends on the WD mass.

Such a He-flash was realized as the He nova V445 Pup (Kato & Hachisu 2003), which was discovered on

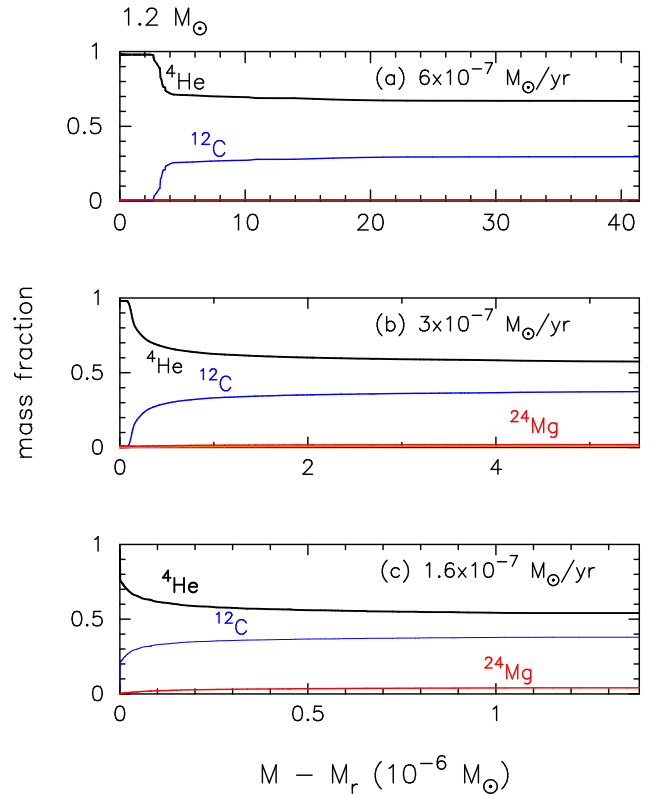


Figure 15. Same as Figure 14, but for the $1.2 M_{\odot}$ WD. (a) M12.6 at $t=2.3$ yr. (b) M12.3 at $t=0.4$ yr. (c) M12.16 at $t=1.9$ day.

UT 2000 December 30 by Kanatsu (Kato & Kanatsu 2000). Unfortunately, the strong dust blackout occurred 210 days after the discovery. The outburst shows unique properties such as the absence of hydrogen and unusually strong carbon emission lines as well as strong emission lines of Na, Fe, Ti, Cr, Si, Mg, and He (Ashok & Banerjee 2003; Iijima & Nakanishi 2007). Kato et al. (2008) estimated the WD mass to be extremely large ($> 1.35 M_{\odot}$) using model light curve fitting. No calculation results on the abundance ratio were published, but the C-rich spectra with He, Si, and Mg lines are broadly consistent with our model of M135.16.

6. DISCUSSION

6.1. Numerical mass-loss rates

In the present paper, we assumed a mass-loss formula in the extended phase of the nova outburst as described in Section 2. This mass-loss formula may not be accurate because we did not take the fitting method as described in Kato et al. (2017a) into consideration. We call our assumed mass-loss rate the numerical mass-loss rate to distinguish it from the real wind mass-loss rate. Here we discuss the effects of the numerical mass-loss rate on the yield of nuclear synthesis.

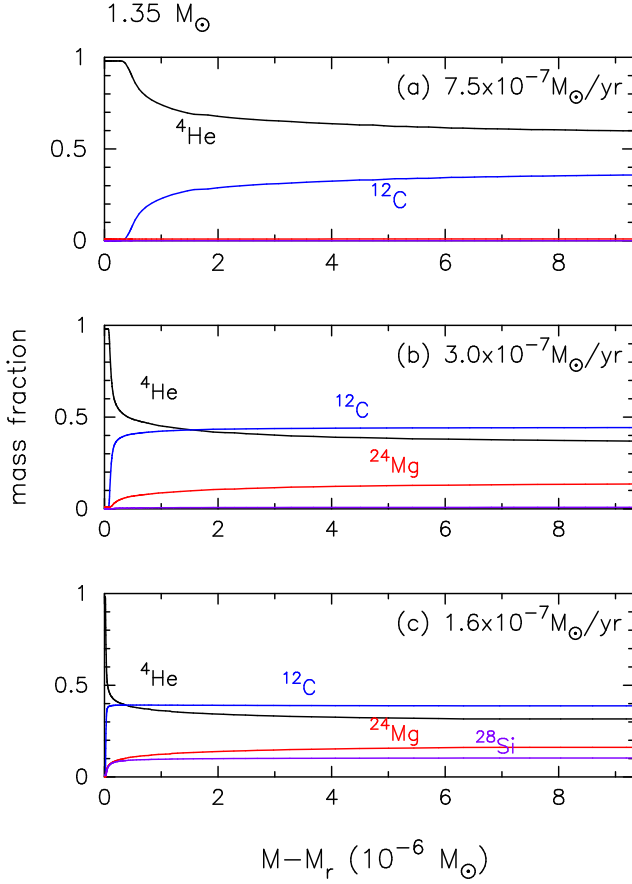


Figure 16. Same as Figure 14, but for the $1.35 M_{\odot}$ WD. (a) M135.75 at $t = 0.46$ yr, (b) M135.3 at $t = 0.29$ yr, (c) M135.16 at $t = 0.14$ yr.

A number of nova light curves have been reproduced theoretically with optically thick winds (e.g., Hachisu & Kato 2006, 2010, 2014, 2015, 2016a,b). The light curves are well explained in terms of free-free emission, which is calculated mainly from the wind mass-loss rate. At the optical maximum, the wind mass-loss rate is the largest and subsequently decreases with time. Thus, the optical light curve decay corresponds to the decreasing mass-loss rate and decreasing envelope mass.

We compare two nova light curves with different mass accretion rates. In the decay phase of the nova outburst, the outbursting envelope approaches steady state. Then the two nova light curves are almost the same, except for the peak brightness. For example, nova 1 has a more massive ignition mass, that is, a larger initial envelope mass, and therefore, has a larger wind mass-loss rate and brighter peak. After Δt from the peak, the envelope mass of nova 1 decreases and becomes equal to that of nova 2 at the peak. So, we have $\Delta t = \Delta M_{\text{acc}} / \dot{M}_{\text{wind}}$, where ΔM_{acc} is the difference of the accreted mass between nova 1 and nova 2 and \dot{M}_{wind} is the mean mass

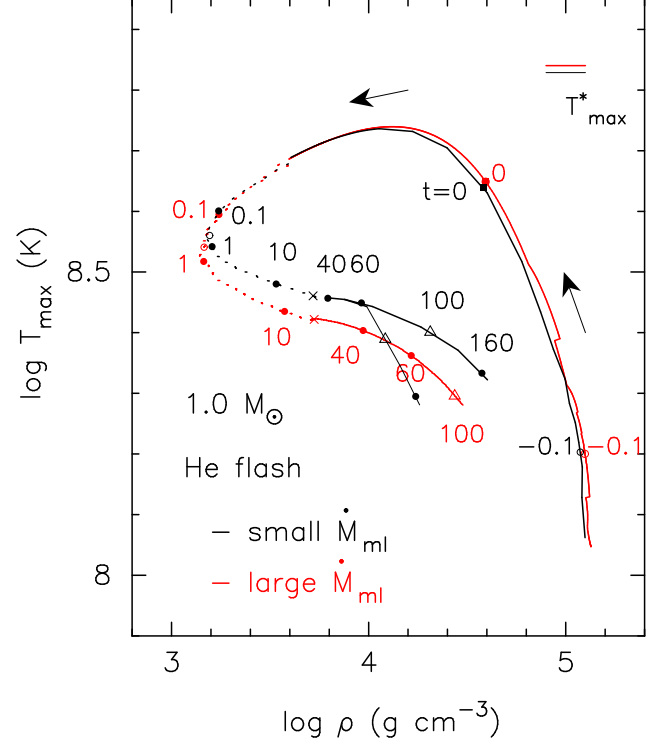


Figure 17. Same as Figure 3, but for two models for the $1.0 M_{\odot}$ WD with the same mass-accretion rate but different mass loss rates; M10.16 (black line) and M10.16.T (red line). Time from $t = 0.0$ (at $L_{\text{nuc}} = L_{\text{nuc}}^{\text{max}}$) is indicated beside the lines in units of years: $t = -0.1$ yr (open circle), 0.0 (filled square), 0.1, 0.5 (open circle), 1, 10, 20 (cross), 40, 60, 100 (open triangle), and 160 yr (M10.16 only).

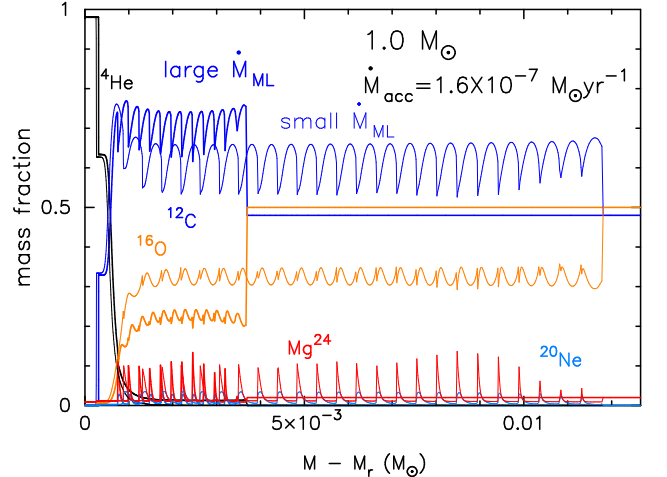


Figure 18. Comparison of the abundance profiles in the surface region of the $1.0 M_{\odot}$ WD models. Thin lines: model M10.16. Thick lines: M10.16.T the model with extremely large mass-loss rates.

loss rate of nova 1 around the peak. As \dot{M}_{wind} is large (because of the initial phase), Δt is small. Thus, the duration of nova 1 is slightly longer than that of nova 2.

Table 1 summarizes our model parameters, in which the nova duration is longer for a larger mass-accretion rate except the 1.35 M_{\odot} cases. This tendency is not consistent with the aforementioned theoretical expectation and indicates that we numerically assumed a larger mass-loss rate for smaller \dot{M}_{acc} models.

In order to examine the effects of a larger numerical mass-loss rate, we have calculated a test model (M10.16.T, T refers to ‘test’) with an extremely large numerical mass-loss rate that is 36 times larger than the maximum rate for M10.16. Table 1 lists its model parameters. Compared with M10.16, the recurrence period and the accreted mass are both increased by 11%. Accordingly, the shell flash becomes stronger but only slightly; L_{nuc} is increased only by a factor of 1.3. This increase is negligibly small compared with the difference between other 1.0 M_{\odot} models.

The locus of the maximum temperature in Figure 17 hardly changes from that of M10.16 in the early phase ($t < 1$ yr). The duration of the outburst is much shorter (about a half) because we assumed a large mass-loss rate. Due to the strong mass loss, the envelope mass quickly decreases and the nuclear burning turns off much earlier (each line ends at $L_{\text{nuc}} = 100 L_{\odot}$). In short, the early phase evolution of the flash (high-temperature period, $\log T$ (K) > 8.6) is hardly affected by the choice of the numerical mass-loss rate, but the later phase evolution becomes short for the larger mass-loss rate.

Such difference in evolution results in different nuclear products. Figure 18 compares the composition profile of the two models. The mass fraction in M10.16T shows 13 peaks in ^{12}C (12 peaks in other nuclei), corresponding to the 13 outbursts. The mass fraction of ^{20}Ne and ^{24}Mg show similar peaks to that of M10.16, because they are produced in the early high-temperature period.

On the other hand, $X(^{12}\text{C})$ is larger in model M10.16T by 0.1, and $X(^{16}\text{O})$ is smaller by the same amount. As explained in Section 3.1, ^{16}O is produced from the reaction $^{12}\text{C} + \alpha$ in $\log T$ (K) $\sim 8.4 - 8.5$. In model M10.16T the temperature quickly drops, so this reaction stops earlier than in M10.16. This is the reason that $X(^{20}\text{Ne})$ and $X(^{24}\text{Mg})$ are almost the same but $X(^{12}\text{C})$ is larger and $X(^{16}\text{O})$ is smaller in model M10.16T.

Thus, if we could assume a smaller mass-loss rate than in Table 1 for smaller mass-accretion models, we expect $X(^{12}\text{C})$ and $X(^{16}\text{O})$ to change by a significant amount but $X(^{20}\text{Ne})$ and $X(^{24}\text{Mg})$ hardly change. Figure 2 shows that $X(^{12}\text{C})$ and $X(^{16}\text{O})$ are almost the same for different mass accretion rates. This suggests that the

period of ^{16}O production (i.e., $\log T$ (K) = 8.45 – 8.5) is almost the same for different mass loss rates (see Figure 3). Thus, we can say that our numerical mass loss assumption is not inappropriate from the viewpoint of nuclear products on the 1.0 M_{\odot} WD. So we conclude that for the 1.0 M_{\odot} WD a small amount of ^{24}Mg is produced, but ^{28}Si is hardly produced.

The same argument can be applied to the 1.2 M_{\odot} models. In models M12.6 and M12.3, the wind phase is relatively short and ^{24}Mg production ($\log T$ (K) $\gtrsim 8.6$) had almost finished until the mass loss started. Thus, our main conclusion is that a small amount of ^{24}Mg is produced and no heavier nuclei production than ^{24}Mg , is still valid.

In the case of M12.16, ^{24}Mg is synthesized mainly in the early stages (Figure 8(b) and (c)). The mass loss starts shortly before stage (b), and the wind mass-loss rate increases with time and reaches a value near maximum in stage (d). Thus, the resultant mass fraction of ^{24}Mg depends on the adopted mass-loss rate. In stage (b), the mass loss rate $\dot{M}_{\text{ML}} = 2.5 \times 10^{-6} M_{\odot} \text{ yr}^{-1}$, is much smaller than the rate of mass reduction due to nuclear burning, which is roughly estimated as $\dot{M}_{\text{nuc}} = L_{\text{nuc}}/\epsilon_{\text{nuc}} = 4.7 \times 10^7 L_{\odot}/10^{18} \text{ erg s}^{-1} = 2.8 \times 10^{-3} M_{\odot} \text{ yr}^{-1}$. Here we simply assume $\epsilon_{\text{nuc}} = 1. \times 10^{18} \text{ erg s}^{-1}$, including nuclear energy generation of He-burning and a part of the burning of the heavier nuclei. In stage (c) the mass loss rate $\dot{M}_{\text{ML}} = 3.2 \times 10^{-5} M_{\odot} \text{ yr}^{-1}$ is also smaller than the nuclear burning rate $\dot{M}_{\text{nuc}} = 2.3 \times 10^{-4} M_{\odot} \text{ yr}^{-1}$. In stage (d) the nuclear burning rate decreases and approaches steady state, and $\dot{M}_{\text{ML}} = 2.7 \times 10^{-4} M_{\odot} \text{ yr}^{-1}$ is much larger than $\dot{M}_{\text{nuc}} = 9.5 \times 10^{-6} M_{\odot} \text{ yr}^{-1}$. Thus, if we assume much larger mass-loss rates than we assumed in the present work, the high-temperature period becomes shorter, and less ^{24}Mg is produced. Inversely, if we assume a smaller mass-loss rate, the period from (b) to (c) does not change, but the period from (c) to (d) becomes longer. Therefore, the production of ^{24}Mg could increase slightly.

Figure 8 shows a small amount of ^{28}Si is produced in the stages (b) and (c). In these stages, the mass-loss rate does not affect evolution, so the production of ^{28}Si is unchanged. Since ^{28}Si production is small, we may conclude that heavier nuclei such as ^{40}Ca are unlikely to be produced.

In the 1.35 M_{\odot} models, ^{28}Si is not produced much for high mass-accretion rates, because the maximum temperature is not sufficiently high. Hence, we do not expect significant production of ^{28}Si and heavier nuclei if we decrease the mass-loss rate. In model M135.16, most of ^{28}Si is synthesized before the mass loss starts ($t = 3$

days in stage (c) in Figure 12). Thus the production of ^{28}Si does not change much with the choice of numerical mass loss rate.

6.2. Comparison of nucleosynthesis with other works

Hashimoto et al. (1983) calculated nucleosynthesis during explosive He-burning with a nuclear reaction network for 181 nuclear species from ^1H through ^{62}Cu , assuming a constant pressure and radiation is dominant. The nuclear products are dominated by ^4He and ^{12}C followed by ^{28}Si and ^{24}Mg , in the model of $\log P$ (dyn cm^{-2}) = 21 at $\log T$ (K) ~ 8.81 and $\log \rho$ (g cm^{-3}) ~ 4.0 . Heavier nuclei are synthesized with higher temperature (^{32}S at $\log T > 8.85$) and ^{36}Ar is produced 0.15 % only at the highest temperature, $\log T = 8.887$. No other heavier nuclei are synthesized. Although their model is based on the so-called one-zone model, these results are consistent with the nuclear products of our M135.16 model. In their model of $\log P$ (dyn cm^{-2}) = 22, ^{40}Ca is produced at a very high temperature $\log T$ (K) > 9.11 , which is not reached in our models (see T_{max} in Table 1). We conclude that ^{40}Ca is hardly synthesized in our $1.35 M_{\odot}$ WD models.

Kamiya (2012) calculated nucleosynthesis in He shell flashes on massive WDs with the so-called one-zone approximation. For his $1.35 M_{\odot}$ WD model with the envelope mass of $3.2 \times 10^{-4} M_{\odot}$, the envelope composition is $Y = 0.42$, $X(^{12}\text{C}) = 0.15$, $X(^{16}\text{O}) = 7.8 \times 10^{-4}$, $X(^{20}\text{Ne}) = 0.0025$, $X(^{24}\text{Mg}) = 0.032$, $X(^{28}\text{Si}) = 0.30$, $X(^{32}\text{S}) = 4.1 \times 10^{-5}$, and $X(^{36}\text{Ar}) = 5.3 \times 10^{-4}$ by mass. The envelope mass ($3.2 \times 10^{-4} M_{\odot}$) is about 2 times and the maximum temperature ($\log T_{\text{max}}$ (K) = 8.92) is much higher than our evolution model M135.16. Thus, the nuclear reaction proceeds up to much heavier elements. In Kamiya's model, the most abundant nuclei are ^{28}Si , followed by ^{12}C , except unburnt helium. This is consistent with the tendency of decreasing (increasing) ^{12}C (^{28}Si) fraction extrapolated from our Models M135.75 and M135.16. Also, the small amounts of ^{16}O and ^{20}Ne are similar to ours. Thus, we regard that our nucleosynthesis is consistent with Kamiya's results.

Kamiya (2012) also showed that ^{40}Ca is hardly synthesized in the WD masses of $< 1.3 M_{\odot}$. For his $1.35 M_{\odot}$ WD model, a very small amount ($\sim 10^{-5}$) of ^{40}Ca is produced for the massive envelope of mass $10^{-3} M_{\odot}$. We cannot directly connect this one-zone model with our calculation, but we may say that a significant amount of ^{40}Ca cannot be synthesized even if we extend our nuclear network to Ca.

Wu et al. (2017) presented long-term evolutions of He-accreting WDs calculated with MESA code including larger nuclear network than ours. Their Figure 6

shows the composition profile when the initial $1.0 M_{\odot}$ WD had grown up to $1.378 M_{\odot}$ and the central carbon burning had just begun after successive He shell flashes with $\dot{M}_{\text{acc}} = 7.5 \times 10^{-7} M_{\odot} \text{ yr}^{-1}$. When the WD mass was $\sim 1.35 M_{\odot}$ (-1.69 in their log mass coordinate), the chemical composition is dominated by ^{12}C and ^{24}Mg , with $X(^{12}\text{C})$ larger than $X(^{24}\text{Mg})$ by several tens of percent. The secondary dominant elements are ^{16}O and ^{20}Ne , that are almost the same value and one order of magnitude smaller than C and Mg. Our model M135.75 (see Figure 11(a), $1.35 M_{\odot}$ with $\dot{M}_{\text{acc}} = 7.5 \times 10^{-7} M_{\odot} \text{ yr}^{-1}$) shows that $X(^{12}\text{C})$ varies around 0.6, $X(^{24}\text{Mg})$ does around 0.3, and both $X(^{16}\text{O})$ and $X(^{20}\text{Ne})$ are several percent. Thus, their results are very consistent with ours. Wu et al. (2017) included 57 reactions up to ^{28}Si , whereas we include 21 reactions also up to ^{28}Si , but both results are quite consistent with each other. Thus, we think that our nuclear reaction network covers the major processes for He flashes.

Wang et al. (2017) presented He-accreting CO WD models. In their pre-central-carbon-ignition model of $1.376 M_{\odot}$ with $\dot{M}_{\text{acc}} = 2 \times 10^{-6} M_{\odot} \text{ yr}^{-1}$, the envelope is enriched by C and O, i.e., $X(^{12}\text{C}) \sim 0.45$ and $X(^{16}\text{O}) \sim 0.4$, with little contamination of Ne (several percent), Mg, Si (< 0.01), and small amount of S (< 0.001). This C/O enrichment for high mass-accretion rate is consistent with our results.

6.3. Comparison with other old calculations

José et al. (1993) calculated He shell flashes with one-zone approximation, i.e. plane-parallel structure with no heat flux between the core and the He layer, using the Kramers opacity. They presented the $\rho - T$ loci for the $1.2 M_{\odot}$ model, similar to our Figure 6. Their loci show similar shapes, but located towards the left and the lower side to our $\rho - T$ loci. This difference can be understood from their approximation. They assumed that no energy is absorbed in the lower layer of the nuclear burning region. This approximation is not good (see Kato et al. 2017a), and tends to weaken the flash. Thus, they obtained lower maximum temperature.

Shara & Prialnik (1994) presented He flash calculations with the old opacity and claimed that Ne/Mg-rich matter accumulates on a $1.25 M_{\odot}$ WD. In their model of $1.25 M_{\odot}$ WD with $\dot{M}_{\text{acc}} = 1 \times 10^{-6} M_{\odot} \text{ yr}^{-1}$, the ignition mass is $\sim 1 \times 10^{-4} M_{\odot}$ and the recurrence period is 100 yr. Their Figure 3 shows that $X(^{12}\text{C})$ and $X(^{24}\text{Mg})$ change with anti-correlation around 0.55 and 0.2 – 0.4, respectively. This anti-correlation and carbon mean fraction is consistent with our tendency in Figure 7(a). However, their extremely large ^{24}Mg fraction ($X(^{24}\text{Mg}) = 0.55$ in the last maximum) is not con-

sistent with the calculations by [Wu et al. \(2017\)](#) and the present work ($X(^{24}\text{Mg}) < 0.15$ in model M12.6).

This overproduction of ^{24}Mg could be a result of the high maximum temperature, $\log T_{\text{max}} (\text{K}) = 8.72$ (see their Figure 2), which seems to be extremely high compared with the tendency of our models in Table 1. Thus, their overproduction could be attributed to inadequately larger mass grids for the nuclear burning region, that is too coarse to resolve the helium-burning layer. Such mass grids that are too large are suggested in their Figure 3 that shows only five peaks in the ^{12}C and ^{24}Mg abundances even after the WD experienced eleven shell flashes (see their Figure 2). This is due to the rezoning process where they combined neighboring several mass grids into one to reduce the total number of mass grids (their referred paper adopted only < 120 mass grids for the total WD). As a result, the abundance profile shows irregular wavy variation. The last peak of $X(^{24}\text{Mg}) \sim 0.55$ is 3.7 times the previous peak $X(^{24}\text{Mg}) = 0.15$. A small number of mass grids ($< \text{a few hundred}$) is insufficient to follow many shell flashes because it should cover rapidly changing nuclear burning region and the expanding outer region (see [Kato et al. \(2017\)](#) for a criticism on their calculation). The very high T_{max} could be explained as a result of coarse grids in the burning layer. We conclude that their claim of a large mass fraction of ^{24}Mg in the $1.25 M_{\odot}$ WD is not real, but a result of too coarse grids calculation.

6.4. Stability line of He-burning

The WD mass on the stability line for an accretion rate is determined as follows. If accretion is started onto a sufficiently less massive WD (in a left side of Figure 1), helium burns stably. The WD mass increases and moves toward the right in Figure 1. After a certain mass is accumulated, helium flashes start to occur. We consider the WD mass when the first flash occurred as the mass of the stability line for the assumed mass accretion rate.

Figure 1 shows the stability line (dashed line) for He shell-burning. We added another stability line (thin purple solid line) taken from Figure 1 of [Wang et al. \(2017\)](#). This line agrees well with our stability line at $M_{\text{WD}} \gtrsim 0.9 M_{\odot}$. The difference of the stability lines in lower mass WDs is probably due to the difference in the stability criterion of different numerical codes. Near the boundary shell flashes are very weak and difficult to draw a clear definition of stability line. In our calculation, we regard an evolution with small amplitude of luminosity pulsations as “stable,” because no shell flashes are triggered. Although there is no detailed description in [Wang et al. \(2017\)](#), we suppose that such

difference in the stability definition is a possible reason for the two different stability lines.

6.5. Maximum temperature

The maximum temperature attained in helium shell flashes is important for nuclear yields. In this subsection, we examine the constraints on the maximum temperature. For a given ignition mass, the theoretical maximum temperature can be obtained as follows. For a plane parallel envelope, the pressure at the bottom can be obtained from a simple integral from the hydrostatic balance, $\delta P / \delta r = GM_{\text{WD}} \rho / R^2$,

$$P = \frac{GM_{\text{WD}} M_{\text{env}}}{4\pi R^4}, \quad (2)$$

where, M_{WD} , R , and M_{env} , are the WD mass, its radius, and mass of the He-rich envelope respectively. We define the maximum temperature T_{max}^* when $P = P_{\text{rad}}$, i.e., neglecting the gas pressure,

$$T_{\text{max}}^* = \left(\frac{GM_{\text{WD}} M_{\text{env}}}{4\pi a R^4} \right)^{1/4}, \quad (3)$$

where T_{max}^* is the theoretical maximum temperature in the extremely radiation dominant plane-parallel atmosphere. This temperature is hardly realized in a hydrostatic WD envelope because the envelope begins to expand and its configuration changes to spherically symmetric and the temperature decreases before the temperature reaches T_{max}^* .

Figure 3 also shows T_{max}^* for each model of $1.0 M_{\odot}$ WD. The maximum value $T_{\text{max}}^{\text{max}}$ is smaller than T_{max}^* by $\Delta \log T (\text{K}) \lesssim 0.11$ (see also Table 1). The maximum temperature $T_{\text{max}}^{\text{max}}$ is closer to T_{max}^* in the $1.2 M_{\odot}$ WD (Figure 6), and slightly larger than that in the $1.35 M_{\odot}$ WD (Figure 10 and Table 1). This means that thermonuclear runaway produces radiation pressure larger than that of the hydrostatic plane-parallel structure. Thus, the envelope structure changes from plane-parallel configuration to spherical and the density decrease in a short time. This expansion timescale is about an hour for M135.16 as shown in Figure 10 (point *a* corresponds $t = 1.7$ hour), which is much longer than the dynamical timescale ($t_{\text{dyn}} \sim 2\pi \sqrt{R^3 / GM_{\text{WD}}} \sim 1$ s).

For a given WD mass, a smaller mass-accretion rate gives a larger ignition mass. If the ignition mass is 10 times larger, the maximum temperature T_{max}^* is $10^{1/4}$ times larger, i.e., it increases by $\Delta \log T_{\text{max}}^* = 0.25$. In the $1.35 M_{\odot}$ WD, the maximum temperature $T_{\text{max}}^{\text{max}}$ is close to T_{max}^* as shown in Figure 10, thus the maximum temperature could reach as high as $\log T (\text{K}) \sim 9.0$ for an ignition mass 10 times larger. For such a high temperature and massive envelope, calcium is synthesized during

He flashes ($X(^{40}\text{Ca}) \gtrsim 10^{-4}$, Kamiya 2012). If we further assume mixing between freshly accreted matter and ashes, we expect much more production of calcium, as discussed in the next section.

6.6. Effect of mixing in the quiescent phase

In the present work we simply assumed that the freshly accreted He matter piled up onto the ashes of previous flashes. However, some mixing may occur between the freshly accreted matter and the ashes during the quiescent phase (i.e., between the two successive outbursts) owing to some mechanism like hydrodynamic instabilities (e.g., Piro 2015).

In our models, the outburst begins at the boundary between the accreted matter $X(^4\text{He})=0.98$ and the leftover ash, i.e., the He ignition starts at $M - M_r = 1.18 \times 10^{-4} M_\odot$ in M135.16 (Figure 12). If the mixing occurs the He-rich matter ($X(^4\text{He})=0.98$) mixes into the ashes and the helium mass fraction at $M - M_r > 1.18 \times 10^{-4} M_\odot$ increase. This makes the helium ignition occur more inside than our models, i.e, the ignition mass becomes larger. As in Section 6.5 a larger ignition mass enables a flash to reach a higher maximum temperature in the nuclear burning region. Thus, nuclear reaction could proceed to more massive nuclei.

Piro (2015) studied turbulent mixing in He-accreting WDs and showed that mixing is greatest at low spin, high accretion rate, and high WD mass. For $1.3 M_\odot$ and $\dot{M}_{\text{acc}} = 1 - 10 \times 10^{-7} M_\odot \text{ yr}^{-1}$, the ashes is mixed with the accreted matter about 0.6-0.8 times the accreted matter by weight.

In order to see how the mixing affects nuclear production, we calculated a test model of $1.35 M_\odot$ with $\dot{M}_{\text{acc}} = 1.6 \times 10^{-7} M_\odot \text{ yr}^{-1}$, i.e., the same parameters as those of model M135.16, but the accreting matter has the chemical composition of $Y = 0.5$, $X(\text{C})=0.14$, $X(\text{Mg})=0.1679$, $X(\text{Si})=0.1765$, assuming the same amount of ash is uniformly mixed with the accreting matter. The ignition mass is $M_{\text{env}} = 1.3 \times 10^{-4} M_\odot$, slightly increased from model M135.16. The maximum temperature reaches $\log T_{\text{max}} = 8.83$, increased by $\Delta \log T = 0.015$. The He-burning ash has the chemical composition of $X(^{12}\text{C})=0.17$, $X(^{24}\text{Mg})=0.18$, $X(^{28}\text{Si})=0.63$, i.e., more carbon and magnesium are processed to silicon than in model M135.16. This can be understood from Table 2, that shows silicon production being sensitive to the maximum temperature. For Ca production, however, we may not expect much, because it is produced in much higher temperature ($\log T$ (K) > 9.0).

We can further consider a case that the accreted matter is not uniformly mixed with the ash, but is di-

vided into many small blobs of the original composition ($X(^4\text{He})=0.98$) that dig into the deep ash and ignite there. In this case, the ignition mass effectively becomes larger. If we roughly assume an ignition mass as twice as large, i.e., the same amount of ash being mixed with the accreted matter, the maximum temperature could be higher by $\Delta \log T \sim (\log 2)/4 = 0.075$ than that in M135.16, from Equation (3). Then, the maximum temperature may reach $\log T = 8.81 + 0.075 = 8.89$. This temperature corresponds to that of a Kamiya's grid model (Kamiya 2012), $M_{\text{WD}} = 1.38 M_\odot$ with $\log M_{\text{env}} \sim -4.0$, that gives $\log X(^{40}\text{Ca}) \sim -6$. Thus, a very small but non-zero amount of Ca could be produced.

For a $1.38 M_\odot$ WD, we may take a model calculation in Kato et al. (2017b) in which the first helium-shell flash occurs after the 1543 successive hydrogen flashes for $\dot{M}_{\text{acc,H}} = 1.6 \times 10^{-7} M_\odot \text{ yr}^{-1}$. The ignition mass is $M_{\text{env,He}} = 7.5 \times 10^{-5} M_\odot$ and the maximum temperature reaches $\log T_{\text{max}} = 8.88$. If we assume that the mixing makes the ignition mass 2 or 3 times larger, the maximum temperature would be close to $\log T_{\text{max}} = 8.96$, and 9.0, respectively. Kamiya's grid models give $\log X(^{40}\text{Ca}) = -5$ to -4 , one order of magnitude larger than in the $1.35 M_\odot$ case. However, the Ca production is very sensitive to the temperature, and then we cannot draw a definite conclusion using Kamiya's one-zone model and Kato et al.'s first He flash model.

6.7. Hydrogen-accreting WDs

In a hydrogen-rich envelope with no mixing of core material, hydrogen burning does not produce massive nuclei such as Si and Ca because of lower maximum temperatures (e.g., $\log T_{\text{max}}(\text{K}) = 8.23$ for $1.38 M_\odot$ Kato et al. 2017b). Thus, we consider a case of He flash with the H-rich layer on top of it. Kato et al. (2017b) calculated successive 1543 H-flashes followed by a first He flash. They stopped calculation in the midway of the He flash owing to numerical difficulties, but showed that the surface hydrogen is mixed into the He burning zone by convection.

Wanajo et al. (1999) calculated one zone model with a nuclear network up to Ca. For an envelope of initial chemical composition of $X(\text{H})= 0.424$, $X(\text{He})= 0.165$, $X(\text{C})= 0.0176$, $X(\text{O})= 0.222$, $X(\text{Ne})= 0.134$, and $X(\text{Mg})= 0.0215$ with $\log T_{\text{max}}$ (K) = 8.86 (their Figure 3), proton capture reactions are active and the final product contains $X(\text{Si})=10^{-3} - 10^{-2}$ and $X(\text{Ca})= 10^{-4}$. Politano et al. (1995) also calculated a $1.35 M_\odot$ model with 95 mass zones, in which the maximum temperature reaches $\log T_{\text{max}}$ (K) = 8.55. The nuclear network covers

up to Ca. They assumed the initial chemical composition of $X(\text{H})=0.365$, $X(\text{He})=0.133$, $X(\text{O})=0.15$, and $X(\text{Ne})=0.249$, and $X(\text{Mg})=0.10$. The final calcium mass fraction slightly increases to $X(\text{Ca})=1.82 \times 10^{-5}$ from the initial value of 1.66×10^{-5} .

Combined these calculation with mixing effects of making ignition mass larger, we expect that a substantial amount of Ca would be produced in a very massive WD like $\gtrsim 1.38 M_{\odot}$. It is however clear that we need further calculations in order to obtain definite conclusions on Ca production.

7. CONCLUSIONS

Our main conclusions are summarized as follows.

1. We present successive helium shell-flash calculations with detailed description of nuclear products on the $1.0 M_{\odot}$, $1.2 M_{\odot}$, and $1.35 M_{\odot}$ WDs with the He mass-accretion rates of $\dot{M}_{\text{acc}} = 1.0 - 7.5 \times 10^{-7} M_{\odot} \text{ yr}^{-1}$. Massive nuclei such as ^{24}Mg and ^{28}Si are produced on more massive WDs with lower mass-accretion rates.
2. A mass-growing WD develops a surface layer as He-burning ash on top of the WD core. This surface layer is

enriched with Mg and Si, depending on the mass accretion rate. The silicon in this surface layer is a possible source of Si II $\lambda 6355$ HVFs that is often observed in SN Ia spectra in early phases.

3. In the He-star donor channel to SNe Ia, in which the WD accretes helium-rich matter, WDs had developed a surface layer enriched by ^{24}Mg and ^{28}Si only when it approaches the Chandrasekhar mass, and possibly a small amount of Ca before the explosion. These could be origins of Si II $\lambda 6355$ and Ca II NIR triplet HVFs.

4. Ejecta of He shell flashes consist mainly of He and C. In the $1.35 M_{\odot}$ WD, the ejecta have $> 30\%$ of helium, $< 40\%$ of carbon, and are enriched with Mg and Si by several percent in relatively low mass-accretion rates. This composition is broadly consistent with C-rich spectra of the helium nova V445 Pup.

The authors thank the anonymous referee for useful suggestions and comments that improve the manuscript. This research has been supported in part by Grants-in-Aid for Scientific Research (15K05026, 16K05289) of the Japan Society for the Promotion of Science.

REFERENCES

- Ashok, N. M., & Banerjee, D. P. K. 2003, *A&A*, 409,1007
- Caughlan, G. R. & Fowler, W. A. 1988, *Atomic Data and Nuclear Data Tables*, 40, 283.
- Childress, M.J., Filippenko, A. V., Ganeshalingam, M., & Schmidt, B. P. 2014, *MNRAS*, 437, 338
- Gerardy, C.L., Höflich, P., Fesen, R. A., et al. 2004, *ApJ*, 607, 391
- Graboske, H. C., Dewitt, H. E.d.; Grossman, A. S., & Cooper, M. S. 1973, *ApJ*, 181, 457
- José, J., Hernanz, M., & Isern, J. 1993, *A&A*, 269, 291
- Hachisu, I., & Kato, M. 2001, *ApJ*, 558, 323
- Hachisu, I., & Kato, M. 2006, *ApJS*, 167, 59
- Hachisu, I., & Kato, M. 2010, *ApJ*, 709, 680
- Hachisu, I., & Kato, M. 2014, *ApJ*, 785, 97
- Hachisu, I., & Kato, M. 2015, *ApJ*, 798, 76
- Hachisu, I., & Kato, M. 2016a, *ApJ*, 816, 26
- Hachisu, I., & Kato, M. 2016b, *ApJS*, 223, 21
- Hachisu, I., Kato, M., & Nomoto, K. 1996, *ApJ*, 470, L97
- Hachisu, I., Kato, M., & Nomoto, K. 1999a, *ApJ*, 522, 487
- Hachisu, I., Kato, M., Nomoto, K., & Umeda, H. 1999b, *ApJ*, 519, 314
- Hashimoto, M.-A., Hanawa, T., & Sugimoto, D. 1983, *PASJ*, 35, 1
- Iben, I., Jr.; MacDonald, J. 1995, *Lecture Notes in Physics*, 443, ed. D. Koester & K. Werner (Springer-Verlag, Berlin), 48
- Iijima,T., & Nakanishi, H. 2008, *A&A*, 482, 865
- Itoh, N., Adachi, T., Nakagawa, M., Kohyama, Y., & Munakata, H. 1989, *ApJ*, 339, 354
- Kamiya, Y. 2012, *Proceedings of the XII International Symposium on Nuclei in the Cosmos (NIC XII)*, 167
- Kato, M., & Hachisu, I. 1994, *ApJ*, 437, 802
- Kato, M., & Hachisu, I. 2003, *ApJ*, 598, L107
- Kato, M., Hachisu, I., Kiyota, S., & Saio, H. 2008, *ApJ*, 684, 1366
- Kato, M., Hachisu, I., & Saio, H. 2017, arXiv: 1711.01529.
- Kato, M., Saio, H., Hachisu, I., & Nomoto, K. 2014, *ApJ*, 793, 136
- Kato, M., Saio, H., & Hachisu, I. 2017a, *ApJ*, 838, 153
- Kato, M., Saio, H., & Hachisu, I. 2017b, *ApJ*, 844,143
- Kato, M., Saio, H., Henze, M. et al. 2016,
- Kato, T., & Kanatsu, K., 2000, *IAU Circ.* 7552
- Mazzali, P. A., Benetti, S., Altavilla, G., et al. 2005, *ApJ*, 623, L37
- Maoz, D., Mannucci, F., & Nelemans, G. 2014, *ARA&A*, 52, 107
- Meng, X., & Han, Z. 2018, *ApJ*, 855, L18
- Mulligan, B. W. & Wheeler, J. C, 2017, *MNRAS*, 467, 778
- Mulligan, B. W. & Wheeler, J. C, 2018, *MNRAS*, 476, 1299
- Nomoto, K. 1982, *ApJ*, 253, 798
- Nomoto, K., Saio, H., Kato, M., & Hachisu, I. 2007, *ApJ*, 663, 1269

- Phillips, M. M. 1993, *ApJ*, 413, L105
- Piersanti, L., Tornambé, A., & Yungelson, L.R. 2014, *MNRAS*, 445, 3239
- Piro, A. L. 2015, *ApJ*, 801, 137
- Politano, M., Starrfield, S., Truran, J. W., Weiss, A., Sparks, W. M. 1995, *ApJ*, 448, 807
- Shara, M. M. & Prialnik, D. 1994, *AJ*, 107, 1542
- Tanaka, M., Mazzali, P. A., Maeda, K., & Nomoto, K. 2006, *ApJ*, 645, 470
- Tanaka, M., Mazzali, P. A., Benetti, S., et al. 2008, *ApJ*, 677, 448
- Umeda, H., Nomoto, K., Kobayashi, C., Hachisu, I., & Kato, M. 1999, *ApJ*, 522, L43
- Umeda, H., Nomoto, K., Yamaoka, H. & Wanajo, S. 1999, *ApJ*, 513, 861
- van Horn, H. M. 1971, in *Proceedings of IAU Symposium No. 42, White Dwarfs*, ed. W. J. Luyten (Springer-Verlag, Dordrecht), 97
- Wanajo, S., Hashimoto, M., & Nomoto, K. 1999, *ApJ*, 523, 409
- Wang, B., Podsiadlowski, P., & Han, Zhanwen 2017, *MNRAS*, 472, 1593
- Wu, C., Wang, B., Liu, D., & Han, Z. 2017, *A&A*, 604, 31
- Zhao, X., Wang, X., Maeda, K., et al. 2015, *ApJS*, 220, 20
- Zhao, X., Maeda, K., Wang, X., et al. 2016, *ApJ*, 826, 211